Artificial Intelligence for Engineering Design, Analysis and Manufacturing

cambridge.org/aie

Artificial intelligence-based Monte-Carlo numerical simulation of aerodynamics of tire grooves using computational fluid dynamics

Ghulam Moeen Uddin[1], Syed Muhammad Arafat[1], Ali Hussain Kazim[1], Muhammad Farhan[1], Sajawal Gul Niazi[1], Nasir Hayat[1], Ibrahim Zeid[2] and Sagar Kamarthi[2]

[1]Mechanical Engineering Department, UET, Lahore 54890, Pakistan and [2]Mechanical and Industrial Engineering Department, Northeastern University, Boston, MA 02115, USA

Research Article

Cite this article: Uddin GM, Arafat SM, Kazim AH, Farhan M, Niazi SG, Hayat N, Zeid I, Kamarthi S (2019). Artificial intelligence-based Monte-Carlo numerical simulation of aerodynamics of tire grooves using computational fluid dynamics. *Artificial Intelligence for Engineering Design, Analysis and Manufacturing* **33**, 302–316. https://doi.org/10.1017/S0890060419000039

Received: 10 June 2018
Revised: 11 February 2019
Accepted: 16 February 2019
First published online: 1 April 2019

Key words:
Artificial Intelligence; computational fluid dynamics; Monte-Carlo simulation; tire grooves; vehicle aerodynamics

Author for correspondence:
Ibrahim Zeid, E-mail: zeid@coe.neu.edu

Abstract

In the current work, the effects of design (groove depth and groove width) and operational (temperature and velocity) parameters on aerodynamic performance parameters (coefficient of drag and coefficient of lift) of an isolated passenger car tire have been investigated. The study is conducted by using neural network-based Monte-Carlo analysis on computational fluid dynamics (CFD). The computer experiments are designed to obtain the causal relationship between tire design, operational, and aerodynamic performance parameters. The Reynolds-averaged Navier–Stokes equations-based Realizable K-ε model has been employed to analyze the variations in flow patterns around an isolated tire. The design parameters are varied over wide range and full factorial design, while considering temperature and velocity is completely explored to draw conclusive results. The multi-layer perceptron type neural network with the back-propagation algorithm is trained to map any non-linearity in causal relationships. The sensitivity analysis is performed to find the relationship between control variables and performance indicators. The importance of control variable is determined by both sensitivity and significance analyses and the paired interaction analysis is performed between selected control variables to find the interactive behavior of corresponding variables. The design parameter of groove width with 6.8% and 41% reduction in drag and lift coefficient, respectively, and conventionally overlooked operational parameter of velocity with 4% and 35% impact on drag and lift coefficient, respectively, are found to be the most significant variables. The air trapped between the longitudinal grooves and the road is found to follow the beam theory. The interaction of the groove depth and width is found to be significant with respect to coefficient of lift based on the air beam concept. The interaction of groove width and velocity is found to be significant with respect to both coefficients of lifts and drag.

Introduction

In last two decades, the aerodynamics of a car gained much more importance with the introduction of energy efficiency legislations, tougher global CO_2 emissions standards, and legislations regarding acoustic levels. Lew *et al.* (2017) studied isolated rotating treaded tire effect on wake plane. They have emphasized the importance of simulation as the test standards set by Worldwide Harmonized Light Vehicles Test Procedures (WLTP). The need for the investigation of relationships between CO_2 emissions and a very long list of vehicle design variables has been recognized by the research community in automotive engineering. Considering every single design variable renders the experimental wind tunnel experimentation to be both very tedious and extremely expensive. Therefore, the WLTP approves the use of computer simulations. Similarly, the standards of car noise level are becoming tougher and tougher every year. The European Union has a scope of reducing car's noise-level phase by phase up to 68 dB in 2024 (European Parliament and Council, 2014).

The research community, recently, has published extensive literature on simulation-based investigations of relationships between vehicle aerodynamics and design variables of isolated components of passenger cars like rims and tires (McManus and Zhang, 2005; Van Den Berg and Zhang, 2009; Schütz, 2013; Haag *et al.*, 2017). The wheels and their housing are among the heavy contributors in car's aerodynamic resistance, that is, ~25% of aerodynamic resistance comes from them (Wickern *et al.*, 1997). Therefore, several research work studies have been conducted to understand the effect of different types of rims, front wings, and tire geometries on cars aerodynamics (Kellar *et al.*, 1999; Mears *et al.*, 2002; Modlinger *et al.*, 2008; Landström *et al.*, 2009; Landström *et al.*, 2010; Landström *et al.*, 2011). The wake plane study of an isolated wheel with translational movement of road using Laser Doppler Anemometry was done by Knowles *et al.* (2002). A comprehensive study of wake

© Cambridge University Press 2019

CAMBRIDGE UNIVERSITY PRESS

vortices of an isolated wheel using unsteady Reynolds-averaged Navier–Stokes equations (RANS) was done by McManus and Zhang (2005). In the previous studies, it is shown that higher levels of details like hub spokes, tire treads, etc., have an impact on the aerodynamics of an isolated wheel (Saddington *et al.*, 2007; Issakhanian *et al.*, 2010; Axerio-Cilies *et al.*, 2012; Axerio-Cilies and Iaccarino, 2012). However, the studies investigating the impact of dimensions of tire profile and thread pattern (Sebben and Landström, 2011; Landstrom *et al.*, 2012; Hobeika *et al.*, 2013) are still very limited and need more focus. Furthermore, scientific investigations on the causal relationship between aerodynamic performance variables and tire design variables in combination with operational variables are almost non-existent in the literature.

Machine learning and artificial intelligence tools like neural networks have recently gained a lot of attention by both research and industrial communities in engineering. Innovative ideas coupling the computer-simulated experiments, machine learning tools, and the statistical analysis techniques have been used successfully and reported by research communities in the fields of HVAC, thermodynamics, tooling and manufacturing, etc. (Hughes, 1999; Liang and Du, 2007; Barberousse *et al.*, 2009; Tsanas and Xifara, 2012; Zhou *et al.*, 2015).

This paper presents neural network-based Monte-Carlo analysis of computational fluid dynamics (CFD) investigations of casual relationships between aerodynamic performance parameter, design parameters, and operational parameters of an isolated passenger car tire. A design of experiment constituting various levels of design parameters (tire tread groove depth and tire tread groove width) and operational parameters (temperature of the surroundings and velocity of tire) is constructed. CFD-based computer-simulated experiments were performed to measure the aerodynamic performance parameters, that is, coefficient of drag (C_d) and coefficient of lift (C_l). A back propagation multi-layer perceptron-type neural network is trained on the data to efficiently map any non-linearity in the causal relationship. Monte-Carlo analysis was conducted on the neural network models to conduct the sensitivity, significance, and paired interaction analyses.

Computer-simulated experimentation

Geometry selection

Fackrell and Harvey reported experimental investigation of wind tunnel-based aerodynamic analysis (C_d, C_l, pressure coefficient, vortices) of an isolated tire geometry (Fackrell and Harvey, 1973, 1975; Fackrell, 1974). Geometry used by Fackrell and Harvey was simplified for numerical analysis by Axon *et al.* (1998). Diasinos *et al.* report that in order to better study the impact of factors like groove dimensions and corner radii, etc., the simplification of model geometry is very useful (Diasinos *et al.*, 2015). Therefore, based on the recommendations of Axon *et al.*, a simplified tire geometry for current experimentation has been deployed as shown in Figure 1. A contact patch of 12.6° is used to simulate contact between tire and road (Heo *et al.*, 2014; Diasinos *et al.*, 2015). The main dimensions of tire model are given in Table 1. The origin point, axis orientations, and symmetry plane used in this entire computer-simulated experimentation is shown in Figure 1a. The groove depth and groove width is shown in Figure 1b. The longitudinal grooves that have been employed on the tire model and the contact patch are shown in Figure 1c, d, respectively. The tire model is created in the CAD software (Solidworks, 2017).

Computational domain

A computational domain (with x–y plane acting as a plane of symmetry and cutting the domain in half) is made as shown in Figure 2. The origin point, axis orientation, and symmetry plane are same for the computational domain as shown in Figure 1a. The dimensions of the computational domain (virtual wind tunnel) are set based on recommendation in the literature (Knowles, 2005; Lanfrit, 2005; Wang *et al.*, 2018). Walls of the domain are set far away from tire model and has no effect on the flow around the geometry. Upstream dimension is $X_1/D =$ 5.5 and downstream dimension $X_2/D = 10.5$. Height of domain is $Y_1/D = 7$ and $Y_2/D = 0$. Width of domain is $Z_1/D = 5$ and $Z_2/D = 5$ where D is the diameter of the tire model. Based on these dimensions, the frontal area of the tire model is 0.65% of domain's frontal area in Y–Z plane. The accuracy of the results depends upon the ratio of frontal area of tire model to frontal area of the computational domain (Das *et al.*, 2013; Blocken and Toparlar, 2015; Collin *et al.*, 2017; Haag *et al.*, 2017). The flow inlet and outlet definitions are given to front and back walls as shown in Figure 2.

Meshing

The meshing of the computational domain is made in Ansys meshing module using the hybrid meshing approach. In order to control the cell generation, refinement zones are introduced near the tire model (Strumolo and Babu, 2000; Abohela *et al.*, 2013). For mesh generation, automatic meshing algorithm approach is applied (Haag *et al.*, 2017). Tetrahedral cells are used to fill the domain including the region of refinement zones (Çengel, 2010). Inflation layers are developed on tire boundary and road surface to capture better flow characteristics (Grabowski *et al.*, 2015; Holder *et al.*, 2018; Wang *et al.*, 2018). Prism cells are used to construct the inflation layers. Contact patch is introduced between the tire geometry and road (Diasinos *et al.*, 2015; Haag *et al.*, 2017). A growth rate of 1.2 (20%) is set at all the interfacing zones so that adjacent cells grow gradually and the computation error is minimized (Ahmad *et al.*, 2010). The meshed computational domain along with the zoomed view of tire model in the computational domain and a zoomed view of inflation layer is shown in Figure 3a. The treatment of tire grooves and the meshed tire geometry before and after the computational domain is split into symmetrical halves that can be seen in Figure 3b.

A comprehensive mesh independence analysis is conducted for both our measures, that is, C_d and C_l. At the start of the mesh independence study, the total number of cells in the whole computational domain (the tire model, the road, the five refinement zones, and the rest of domain) were 1 million. The number of cells in the refinement zones are systematically increased by reducing the size of the cells to assess the percentage relative error in the computed values of C_d and C_l. The systematic increase in the number of cells was continued till the percentage relative error is reduced below 3% (Ahmad *et al.*, 2010; Diasinos *et al.*, 2015). The results with 8, 9, and 10 million cells in the mesh independence analysis showed that the percentage relative error for drag and lift was reduced to an acceptable range of below 2%. Further increase in the number of cells will lead to a high computational cost without any significant improvement in the computational accuracy. The final selected computational domain after the mesh independence analysis constituted 9 million cells with majority of the cells confined within the refinement zones.

https://doi.org/10.1017/S0890060419000039 Published online by Cambridge University Press

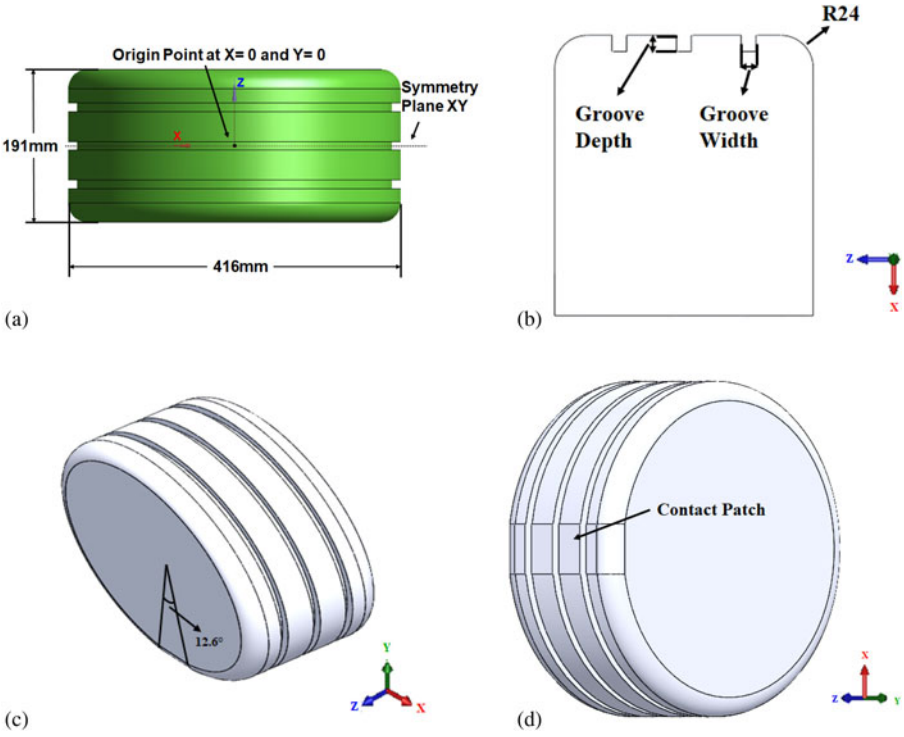


Fig. 1. (a) Tire model dimensions, origin axis, and symmetry plane. (b) Groove dimensions. (c) 3D tire model with longitudinal grooves. (d) Tire contact patch attached to road.

Table 1. The main dimensions of tire model

Diameter (mm)	Width (mm)	Shoulder radii (mm)	Contact patch angle (deg)
416	191	24	12.6

Numerical model configuration

Results from Shih *et al.* (1995) depict that the two-equation Realizable K-ε model is a robust model and it has the ability to accomplish high accuracy for rotating and separating flows. Both the rotating and the separating flow phenomena occur in our computer-simulated experiments. The comparison between different turbulence models on tire model is given by Diasinos *et al.* (2015). The Realizable K-ε RANS model is used to solve complex flows by different studies (Doig and Barber, 2011; Blocken and Toparlar, 2015; Diasinos *et al.*, 2017). The significance of Unsteady Reynolds-averaged Navier–Stokes equations (URANS) cannot be undermined. However, previous research work has reported that steady-state incompressible RANS model can be used without compromising much accuracy (Hobeika *et al.*, 2013; Vdovin *et al.*, 2013; Heo *et al.*, 2014; Diasinos *et al.*, 2015). Furthermore, steady RANS has been reported as still being the most used and accepted approach in vehicle industry (Diasinos *et al.*, 2015). Therefore, steady-state analysis is conducted in this research work as this remains the preferred approach in academia and in industry (Defraeye *et al.*, 2010; Diasinos *et al.*, 2014; Dang *et al.*, 2015; Diasinos *et al.*, 2017). The solution is set as implicit and a finite volume method is used to solve RANS equation (McManus and Zhang, 2005). For pressure and velocity coupling, the coupled algorithm is used as it is more robust and performs well as compared with the segregated solution scheme (Hobeika *et al.*, 2013; Ansys, 2016). Equations are discretized as first-order upwind scheme for the first 400 iterations so that the computational domain can be filled with numbers. First-order upwind scheme can converge in much less amount of time but is less accurate than the second-order upwind scheme. Therefore, after the first 400 iterations, the solution is further run with second-order upwind scheme till the results obtained meet the convergence criteria (McManus and Zhang, 2005; Gérardin *et al.*, 2014). The solution is considered as converged when residual of energy terms reach the value of $\leq 10^{-6}$, residual of velocity (x, y, and z) reach the value of $\leq 10^{-8}$, and residual of continuity reach the value of $\leq 10^{-5}$ (Diasinos *et al.*, 2015). All other solver settings can be found in the guide lines of Ansys Fluent (Ansys, 2016).

Boundary conditions

The rotation of tire model is simulated by the moving wall approach (McManus and Zhang, 2005). Turbulence intensity of the freestream is set to 0.2% (Watkins *et al.*, 1995). A linear (translational velocity) is assigned to the inlet air flow (which is velocity inlet boundary) in negative "x" direction. An angular (rotational) velocity (ω_z) is assigned to the tire in negative "z" direction, as shown in Figure 4a. At the outlet wall (which is pressure outlet boundary), a gauge pressure of zero is set. The road is specified with a no slip boundary condition to simulate the contact between the road and the tire (McManus and Zhang, 2005). The result containing pressure contour plot on the tire model for a selected computer-simulated experiment is shown in Figure 4b.

Process modeling

The design of experiments

The basic level of comparison between the slick and the grooved tire's coefficients of drag and lift has been reported in the previous research work (Hobeika *et al.*, 2013; Leśniewicz *et al.*, 2014). But there is a need of a detailed study which can give answers to

https://doi.org/10.1017/S0890060419000039 Published online by Cambridge University Press

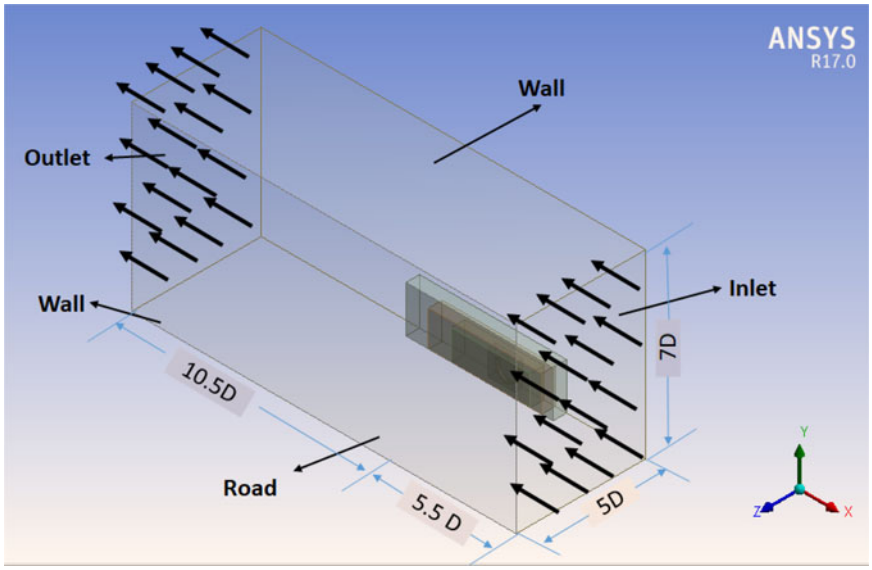


Fig. 2. Computational domain (virtual wind tunnel) for the computer-simulated experimentation.

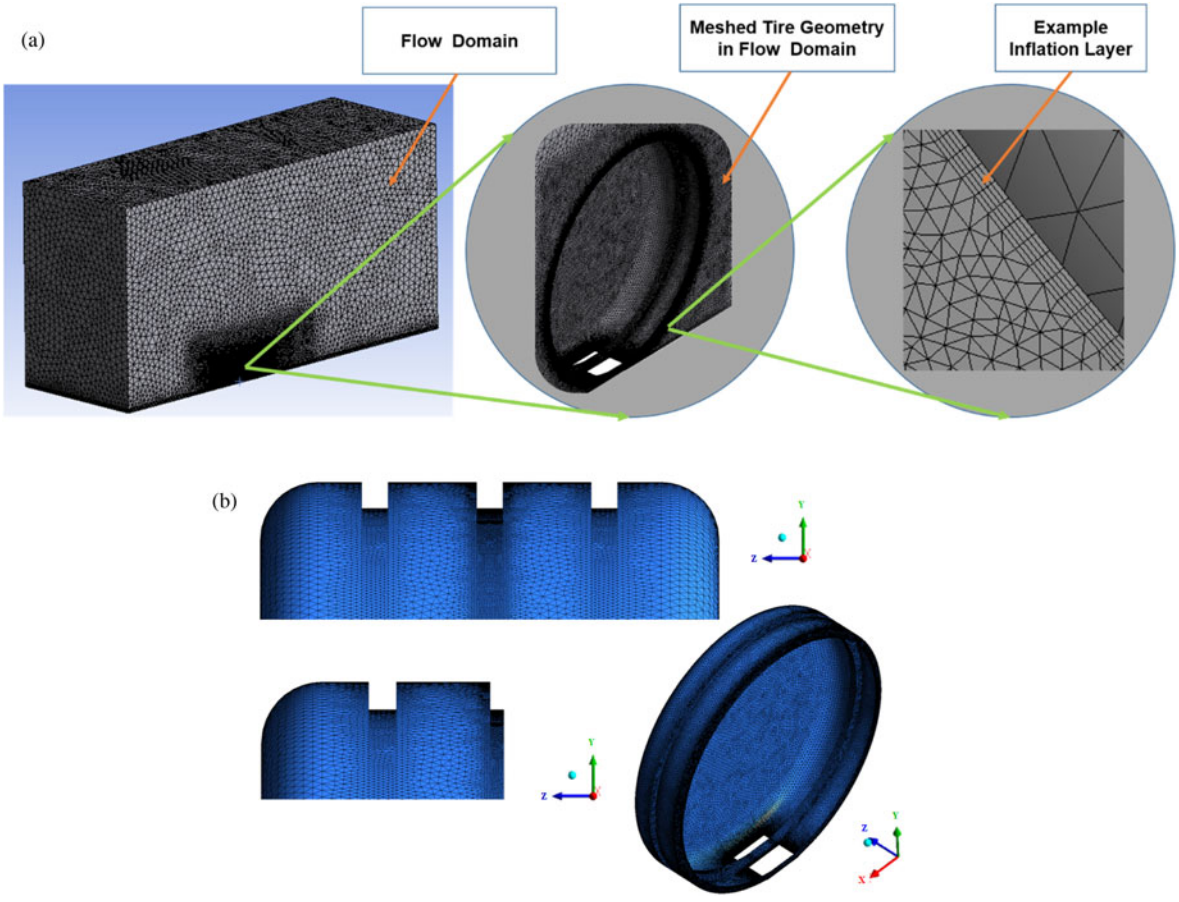


Fig. 3. (a) Meshed computational domain, the zoomed view of tire model, and inflation layer at the interface of the tire model with immediate next zone of the computational domain. (b) The treatment of tire grooves before and after symmetrical halves.

questions like how lift and drag are affected by changing groove depth or groove width. Furthermore, the effect of temperature and velocity on coefficients of drag and coefficients of lift need to be investigated alongside the varying groove width and groove depth.

A full factorial computer-simulated experimental study answering the aforementioned questions is presented in this research work. The main geometry of tire remains unchanged. Four control variables are considered, that is, groove depth (x_1), groove width (x_2), temperature (x_3), and freestream velocity (x_4), maintaining all other conditions constant. The full factorial design of experiments was constructed based on seven levels of groove depth, seven levels of groove width, two levels of

https://doi.org/10.1017/S0890060419000039 Published online by Cambridge University Press

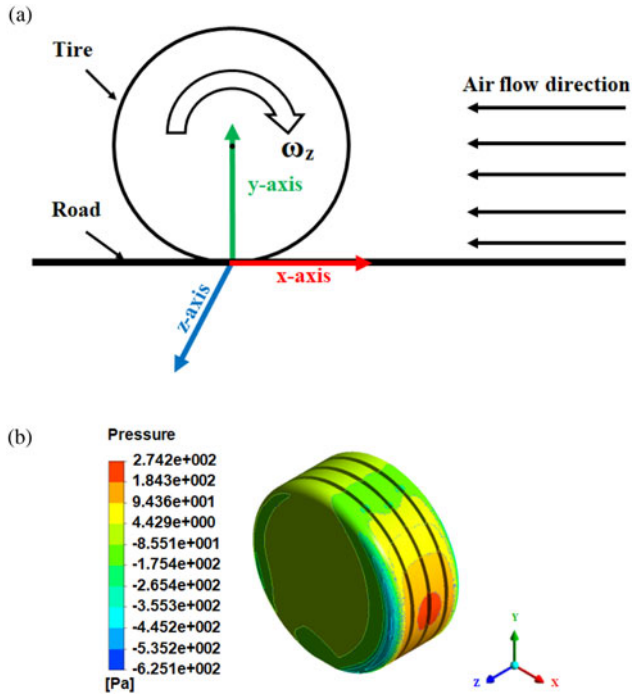


Fig. 4. (a) The rotational motion of tire (ω_z) and direction of air flow. (b) The pressure contour plot on tire model.

temperature, and four levels of velocity. The configuration of the input space of the full factorial design of experiment is shown in Table 2. The design constituted 392 computer-simulated experiments. C_d and C_l are two output variables.

Artificial neural network

Artificial neural networks (ANN) are well known for their ability to map any extent of non-linearity in the data (Uddin *et al.*, 2013; Uddin *et al.*, 2015*a*). Therefore, gradient descent back propagation algorithm-based multi-layer perceptron (MLP)-type ANN are deployed as process models for the computer-simulated design of experiments shown in Table 2. The variables x_1, x_2, x_3, and x_4 are fed to ANN as inputs and variables C_d and C_l are fed as outputs for the neural network training, testing, and validation. The configuration of 4-12-1 (input-hidden-output layer neurons) is employed in the development of MLPs. A learning rate of 0.01 is set for the MLP training. A tangent hyperbolic function is deployed for the forward movement of signal at the nodes of hidden and output layers and gradient decent algorithm is applied for error convergence. The networks are set to train for 10,000 epochs and stopping criterion of 0.0000001 as change in error or no change in error for 2,000 epochs are set. A split of 80%, 10%, and 10% is set for training, testing, and validation of the MLPs. Figure 5 presents a generic diagram of MLPs employed in our study. The MLP-based ANN configuration is summarized in Table 3.

Monte-Carlo experimentation

Monte-Carlo experiments are used to study the causal relationship between the control variables and the output variables using the trained MLP computer models (Uddin *et al.*, 2013, 2015*a*, 2015*b*). In this research work, three types of MLP-assisted Monte-Carlo analyses are being presented, that is, sensitivity analysis, significance analysis, and paired interaction analysis. The details of Monte-Carlo experiments for sensitivity, significance, and paired interaction analyses are given below:

Table 2. Variables and their corresponding levels for the full factorial design of experiment

Variables	Levels	Total number of experiments in full factorial design
[a]Groove depth (mm), x_1	6, 7, 8, 9, 10, 11, 12	7 × 7 × 2 × 4 = 392
[a]Groove width (mm), x_2	6, 7, 8, 9, 10, 11, 12	
Temperature (°C), x_3	15, 40	
[a]Velocity (m/s) , x_4	18.6, 24.2, 30.6, 33.3	

[a](Leśniewicz *et al.*, 2016; Dieselnet, 2018, Maxxis, 2018).

Monte-Carlo experiment 1: factor-wise sensitivity analysis

(1) Four control variables are selected in this experiment, that is, groove depth, groove width, temperature, and velocity. Let x_i represent a control variable where $i = 1,2,3,4$. x_1 = groove depth, x_2 = groove width, x_3 = temperature, and x_4 = velocity. Two output variables which are performance variables are represented by y_1 and y_2.

(2) x_i is varied at regular intervals between its minimum value and its maximum value and n experimental treatments are created. Each varied value of x_i is represented by x_{ik} where $k = 1,2,3 \ldots, n$. All other control variables are represented by x_j where $j = 1,2,3,4$ and $j \neq i$ are kept constant at their respective mid values. The k^{th} input vector for first control variable can be represented as (x_{1k}, x_{2mid}, x_{3mid}, x_{4mid}) and respective output vector is represented by y_{1k} and y_{2k}.

(3) M replications are created for each treatment of k. For each subset of M replications, x_{ik} is kept constant while all other control variables (x_j where $j \neq i$) are perturbed about their mean value. The perturbations are created based on a Gaussian noise with mean equal to zero and standard deviation equal to 1% of x_{jmin} and added to x_{jmid} of each control variable x_j.

(4) The ANN-based computer-simulated model is used to find the response of x_{ik} for n experimental treatments where each experimental treatment constitutes M replications. The responses are obtained in the form of y_{1ikm} and y_{2ikm} where $k = 1,2,3,\ldots,n$ and $m = 1,2,3,\ldots,M$. A Gaussian noise is added to the obtained responses to account for the error in ANN-based computer-simulated model. This Gaussian noise is obtained from $N(\mu_{ne}, \sigma_{ne})$. The μ_{ne} and σ_{ne} are mean and standard deviation of the ANN-based computer-simulated model's prediction error.

(5) From each y_{1ikm} and y_{2ikm} where $m = 1,2,3,\ldots,M$ mean (μ_{1ik} and μ_{2ik} respectively) and standard deviation (σ_{1ik} and σ_{2ik}, respectively) are calculated.

(6) The mean, upper control limit (UCL), and lower control limit (LCL) trend lines for y_1 are obtained from (μ_{1ik}), ($\mu_{1ik} + 3\sigma_{1ik}$), and ($\mu_{1ik} - 3\sigma_{1ik}$), respectively. Similarly, the counterparts of y_2 are used for its mean, UCL, and LCL trend lines.

Monte-Carlo experiment 2: significance analysis

Repeat the steps from 1 to 5 as discussed in "Monte-Carlo experiment 1: factor-wise sensitivity analysis" with an exception in step number 3 which is as follows:

https://doi.org/10.1017/S0890060419000039 Published online by Cambridge University Press

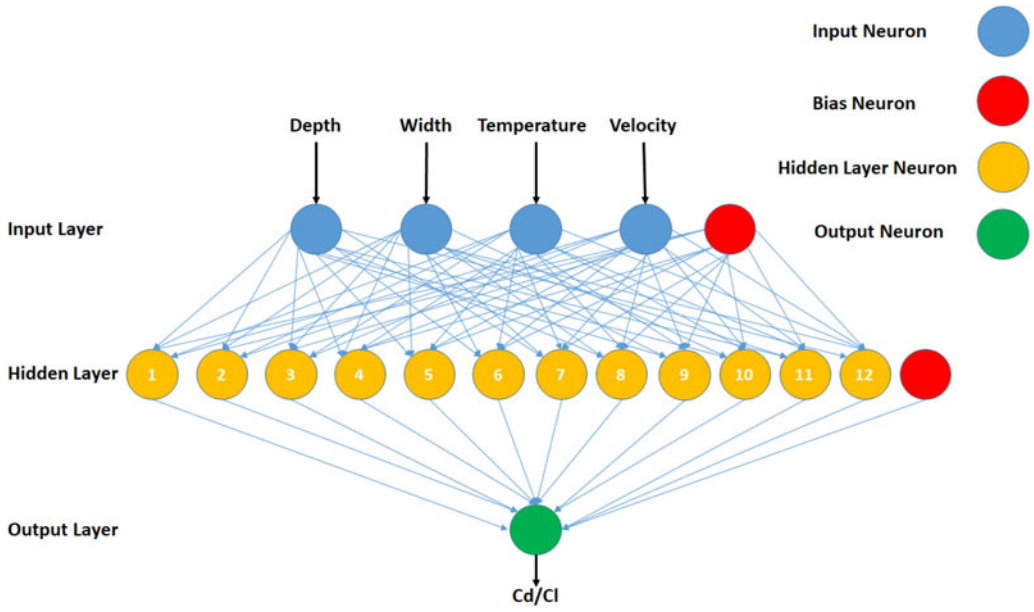


Fig. 5. Generic diagram of MLPs for C_d and C_l.

Table 3. Summary of ANN configuration

ANN configuration	
Algorithm	Gradient descent with back propagation algorithm with multi-layer perceptron
Number of hidden layers	1
Input-hidden-output layer neurons	4-12-1
Learning rate	0.01
Layer function	Tangent hyperbolic

x_{ik} is kept constant for each k value while generating M replications of each kth treatment. All control variables x_j are randomly varied between their respective minimum and maximum values for the whole data set.

Monte-Carlo experiment 2: paired interaction analysis

Repeat the steps from 1 to 5 as discussed in "Monte-Carlo experiment 1: factor-wise sensitivity analysis" with an exception in step number 3 which is as follows:

x_{ik} is kept constant for each k value while generating M replications of each kth treatment. Its pair control variable x_j is randomly varied between its minimum and maximum value and remaining control variables x_j are kept at their respective middle value for whole data set.

Results and discussion

The results presented in this section are based on computer-simulated experiments, MLP-based neural network process model, and Monte-Carlo analysis.

Artificial neural network results

The data set constituting 392 data points each representing four control variables and two output variables, that is, C_d and C_l is used to prepare neural network computer models. Two separate MLPs are trained for C_d and C_l. The effectiveness of the neural network computer model was decided based on the goodness-of-fit criteria (the R^2 for training data subset, the R^2 for testing data subset, and the R^2 for validation data subset). The R^2 values (in case of C_d) for training, testing, and validation are 0.922, 0.946, and 0.928, respectively. The R^2 values (in case of C_l) for training, testing, and validation are 0.962, 0.979, and 0.976, respectively.

The trend line of error reduction in MLP with number of training epochs is shown in Figure 6. Both C_d neural network model shown in Figure 6a and C_l neural network model shown in Figure 6b present a steady error convergence for 10,000 epochs. The training and testing error of the MLP decrease significantly for first 4000 epochs after which a steady decrease is observed. Therefore, if both the networks are further trained, they will only decrease error marginally.

Factor-wise sensitivity and significance analysis

In this section, the sensitivity and significance analyses present the behavior and importance of a control variable with respect to co-responding output variable. The sensitivity analysis studies the trend of a particular output variable against a control variable by varying the concerned control variable at regular intervals and keeping all other variables at their mid values. Further in order to test the robustness of the neural network computer models, 10 replications of each data points are created by adding 1% Gaussian noise. The significance analysis studies the role played by a particular variable in determining an output variable by changing concerned control variable at regular intervals and all other control variables randomly between their minimum and maximum values, respectively. The graph of sensitivity trend of a particular variable can be assessed based on the gradient of its mean trend line. In case of significance trend; if the shape of the corresponding sensitivity trend is retained in significance graph (mean, UCL, and LCL) of a particular variable, then that

https://doi.org/10.1017/S0890060419000039 Published online by Cambridge University Press

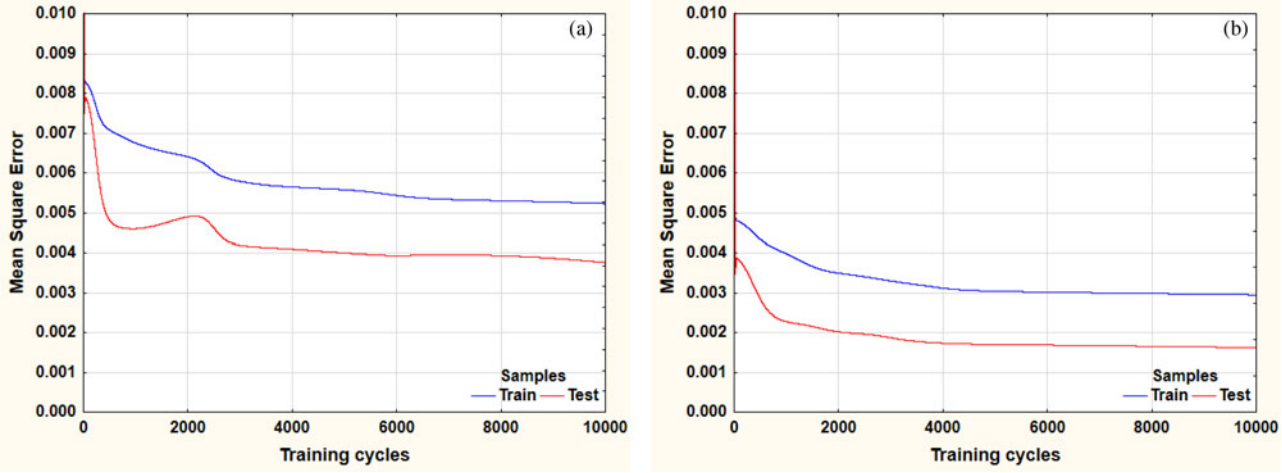


Fig. 6. (a) Training graph for (MLP 4-12-1) drag coefficient case. (b) Training graph for (MLP 4-12-1) lift coefficient case.

particular variable has a stronger causal relationship with output variable. Furthermore, the extent of widening of the confidence interval of a particular variable in its significance trend reflects its strength in comparison with its peer control variables.

Groove depth

The sensitivity trend of C_d with respect to the groove depth is shown in Figure 7a. A steady and significant reduction (~3.2%) in C_d can be achieved by increasing the groove depth up to 11 mm. However, increasing the groove depth beyond that point would not contribute any significant saving in the C_d.

The significance trend of C_d with respect to the groove depth is shown in Figure 7b. The reduction gradient of the significance trend of C_d between the groove depth up to 11 mm is ~2.2%. The random variations in the peer control variables of groove depth (groove width, temperature, and velocity) appear to significantly reduce the gradient of the trend. Moreover, the confidence interval, that is, the gap between UCL and LCL widens. This reinforces the possibility of some other control variables being more significant than groove depth.

The sensitivity trend of C_l with respect to the groove depth is shown in Figure 8a. A steady and significant reduction (~21%) in C_l can be achieved by increasing the depth of groove up to 11 mm. However, increasing the groove depth beyond that point would not contribute any significant reduction in the C_l. This behavior of C_l with respect to groove depth is identical to the corresponding behavior of C_d with respect to groove depth.

The significance trend of C_l with respect to the groove depth is shown in Figure 8b. The random variations in the peer control variables of groove depth (groove width, temperature, and velocity) appear to significantly reduce the gradient of the trend. The confidence interval, that is, the gap between UCL and LCL widens as the groove depth increases. Again the widening of the UCL–LCL gap at higher values of groove depth for C_l is identical to the corresponding behavior of the significance trend of C_d.

Groove width

The sensitivity trend of C_d with respect to the groove width is shown in Figure 9a. A steady and significant reduction (~6.8%) in C_d can be achieved by increasing the width of groove from 7 to 12 mm. The sensitivity trend suggests that by increasing the groove width beyond 12 mm may further reduce C_d and contribute in further savings.

The significance trend of C_d with respect to the groove width is shown in Figure 9b. The reduction gradient of the significance trend of C_d between the groove width of 7–12 mm is ~5.4%. The random variations in the peer control variables of groove width (groove depth, temperature, and velocity) appear to have almost no effect on the gradient of the trend. The gap between UCL and LCL tends to retain its width from mean trend line throughout the range, that is, from 6 to 12 mm. The comparison between Figures 7b, 9b confirms that the groove width is significantly stronger variable.

The sensitivity trend of C_l with respect to the groove width is shown in Figure 10a. A steady and significant reduction (~41%) in C_l can be achieved by increasing the width of groove from 6 to 12 mm. The sensitivity trend suggests that by increasing the groove width beyond 12 mm may further reduce C_l.

The significance trend of C_l with respect to the groove width is shown in Figure 10b. The random variations in the peer control variables of groove width (groove depth, temperature, and velocity) appear to have no effect on the gradient of the trend. The gap between UCL and LCL tends to retain its width with mean throughout the experimental range. The comparison between Figures 8b, 10b also confirms that the groove width is almost twice as significant variable than the groove depth.

Temperature

The sensitivity trend of C_d with respect to the temperature is shown in Figure 11a. A nearly constant reduction (~0.7%) in C_d can be observed by increasing the temperature between 15°C and 40°C. The trend also depicts that increasing the temperature to the range of 50°C–55°C may only reduce the C_d to 1%.

The significance trend of C_d with respect to the temperature is shown in Figure 11b. The gradient of the mean line in Figure 11b between 15°C and 40°C is ~1.3%. The random variations in the peer control variables of temperature (groove depth, groove width, and velocity) appear to have no effect on the gradient of the trend. The gap between upper UCL and LCL widens as the temperature increases. Therefore, irrespective of the weak gradient of temperature, its impact on the C_d remains.

The sensitivity trend of C_l with respect to the temperature is shown in Figure 12a. A steady reduction (~4.2%) in C_d can be observed by increasing the temperature.

https://doi.org/10.1017/S0890060419000039 Published online by Cambridge University Press

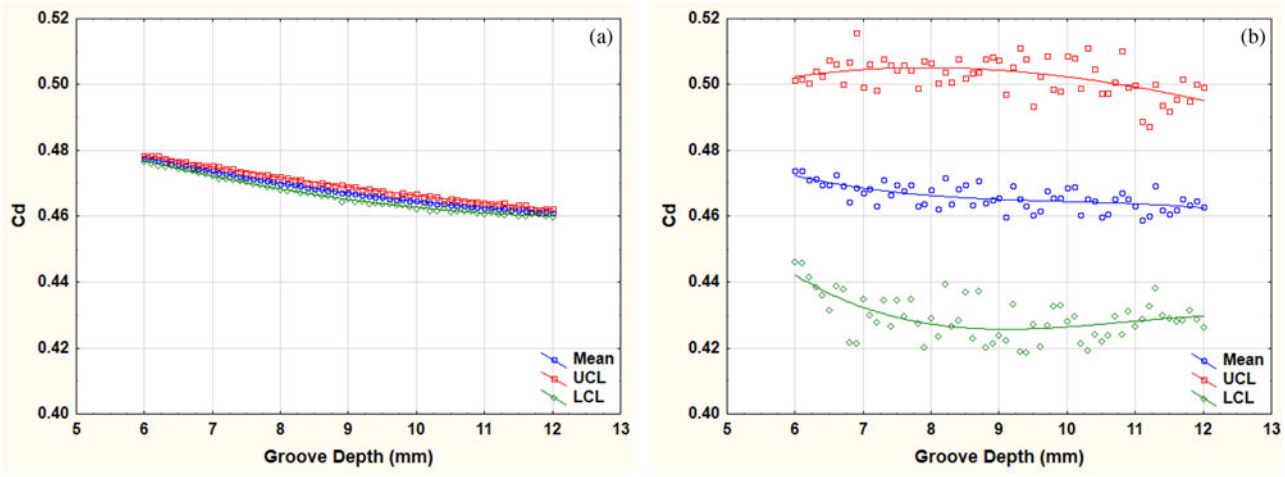


Fig. 7. (a) C_d versus groove depth in sensitivity analysis and (b) C_d versus groove depth in significance analysis.

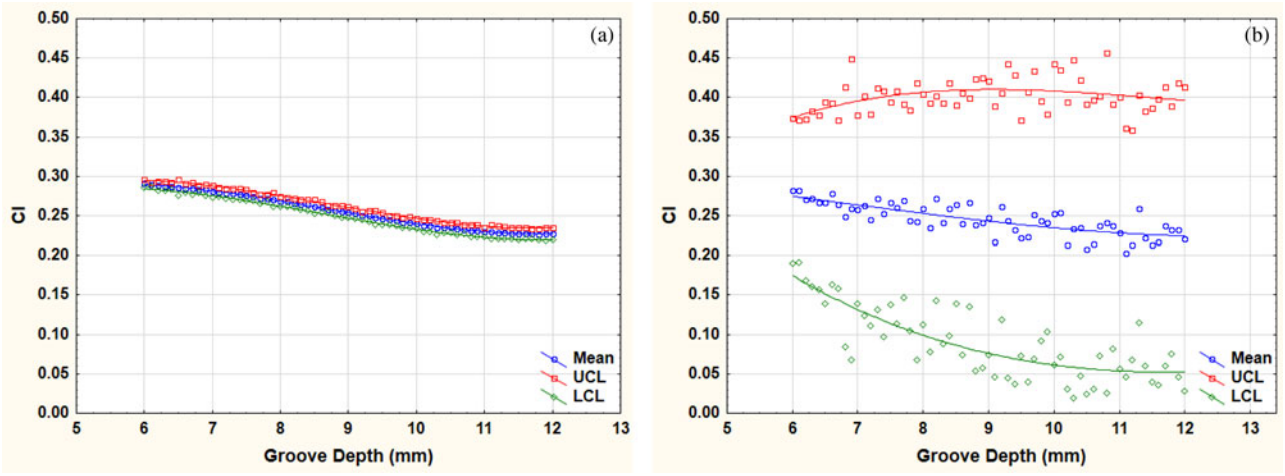


Fig. 8. (a) C_l versus groove depth in sensitivity analysis and (b) C_l versus groove depth in significance analysis.

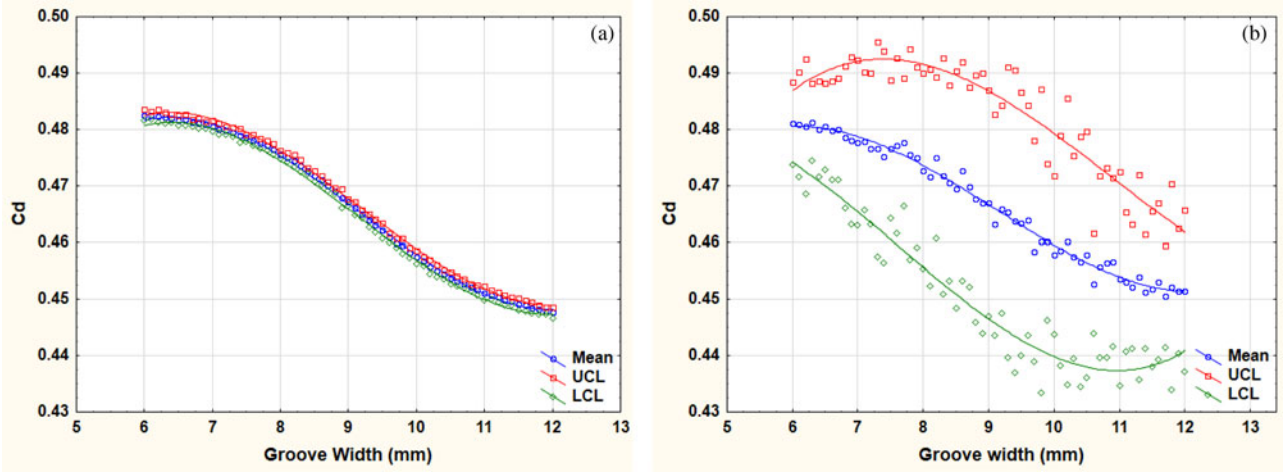


Fig. 9. (a) C_d versus groove width in sensitivity analysis and (b) C_d versus groove width in significance analysis.

The significance trend of C_l with respect to the temperature is shown in Figure 12b. The gradient of the mean line in Figure 12b between 15°C and 40°C is ~10%. The random variations in the peer control variables of temperature (groove depth, groove width, and velocity) appear to have no effect on the gradient of the trend. The gap between upper UCL and

https://doi.org/10.1017/S0890060419000039 Published online by Cambridge University Press

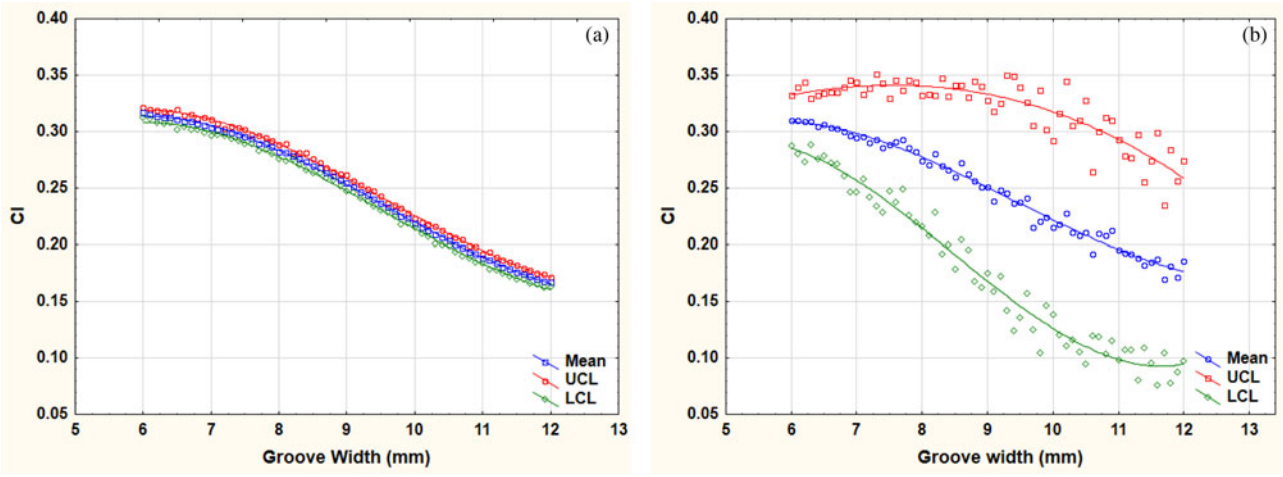


Fig. 10. (a) C_l versus groove width in sensitivity analysis and (b) C_l versus groove width in significance analysis.

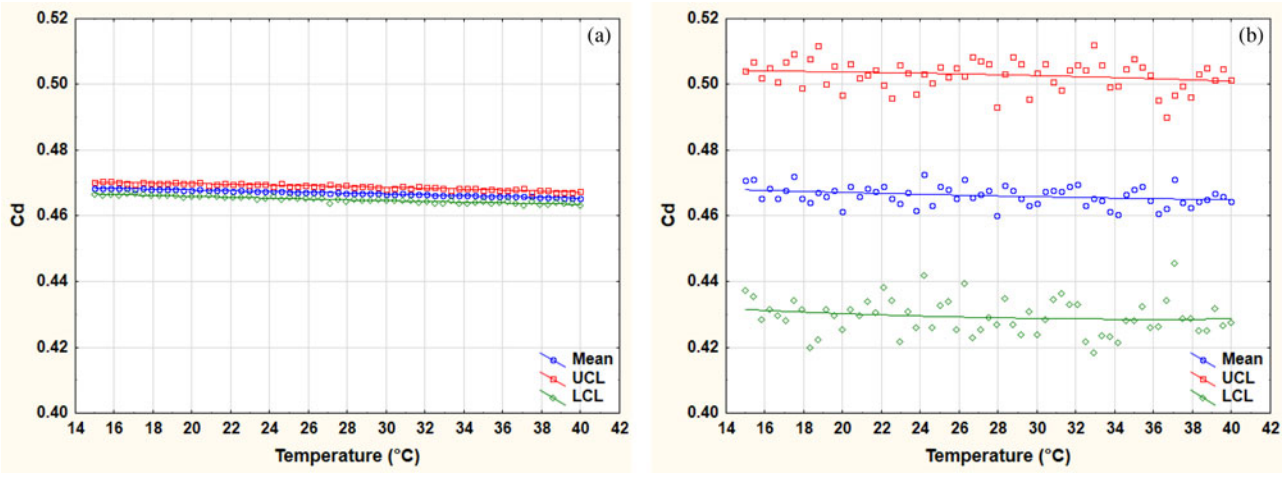


Fig. 11. (a) C_d versus surrounding temperature in sensitivity analysis and (b) C_d versus surrounding temperature in significance analysis.

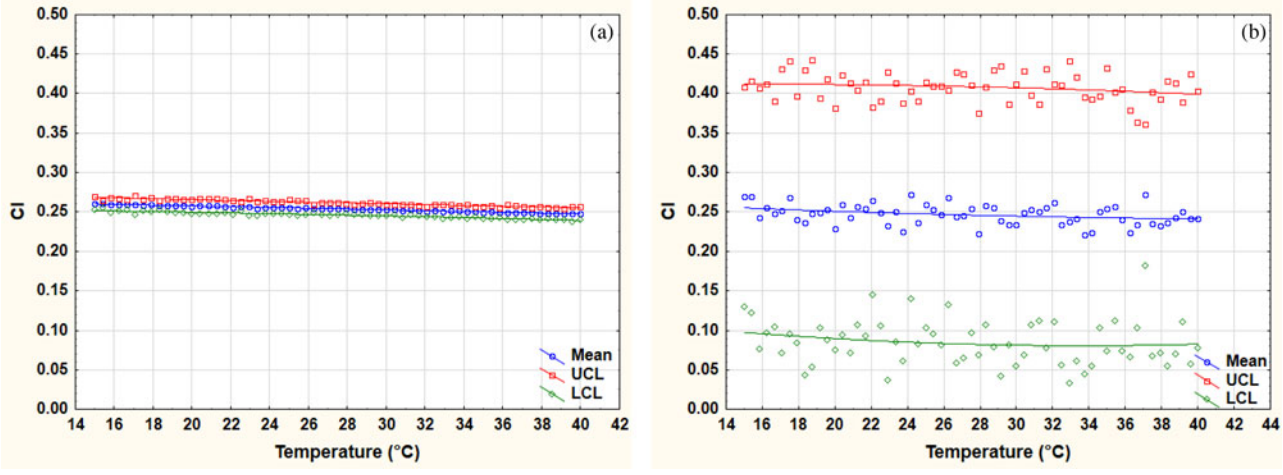


Fig. 12. (a) C_l versus surrounding temperature in sensitivity analysis and (b) C_l versus surrounding temperature in significance analysis.

LCL widens as the temperature increases. Therefore, irrespective of the weak gradient of temperature, its impact on the C_l remains.

Velocity

The sensitivity trend of C_d with respect to the velocity is shown in Figure 13a. A steady and significant increase (~3.9%) in C_d is

https://doi.org/10.1017/S0890060419000039 Published online by Cambridge University Press

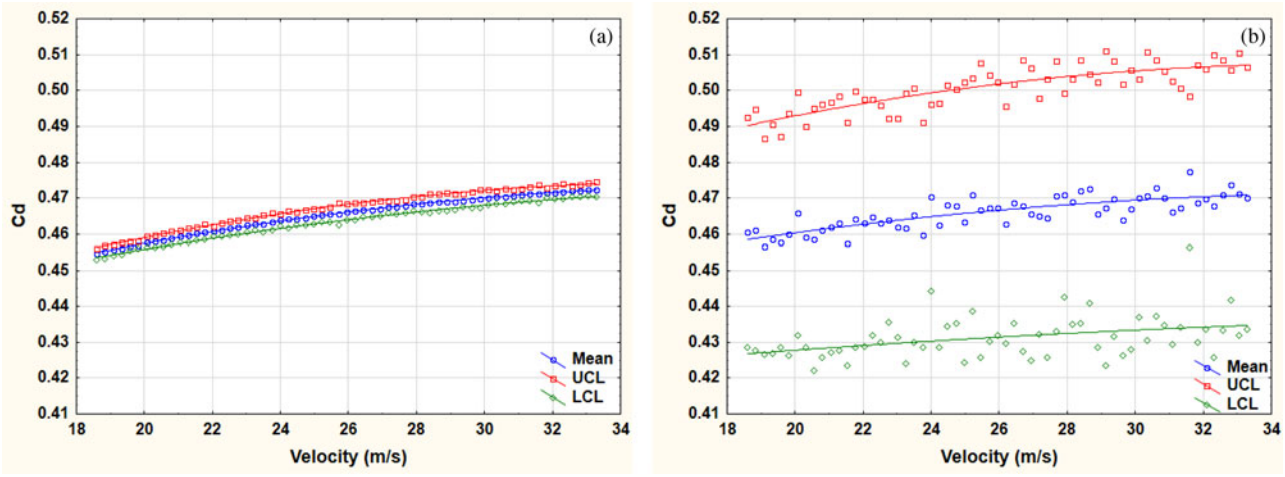


Fig. 13. (a) C_d versus tire velocity in sensitivity analysis and (b) C_d versus tire velocity in significance analysis.

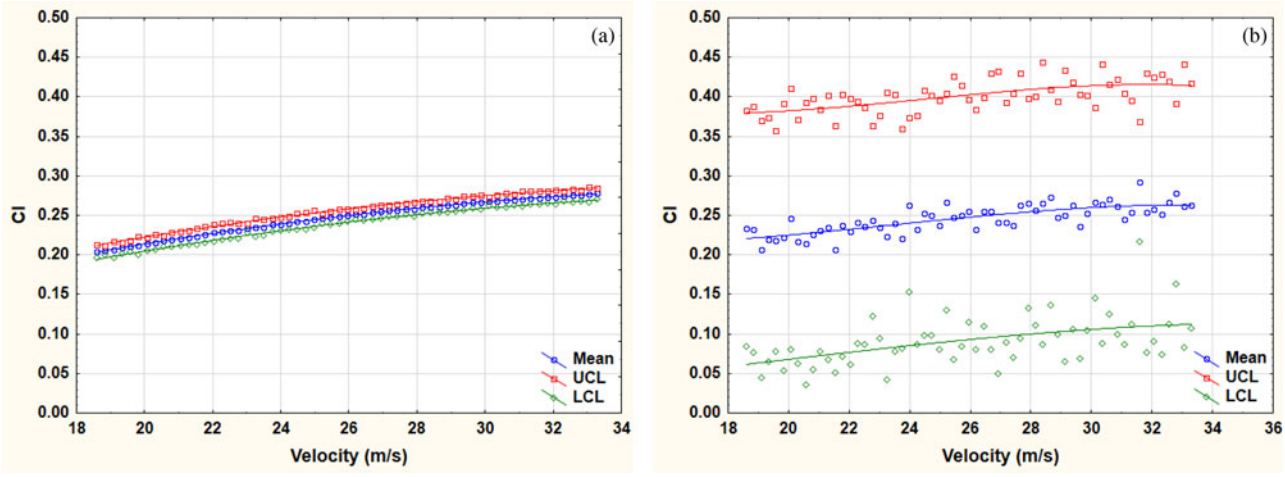


Fig. 14. (a) C_l versus tire velocity in sensitivity analysis and (b) C_l versus tire velocity in significance analysis.

observed by increasing the velocity. The sensitivity trend suggests that by increasing the velocity beyond 33 m/s, a further increase C_d can be expected.

The significance trend of C_d with respect to the velocity is shown in Figure 13b. The gradient increase of the significance trend of C_d between the velocity values 18.6 and 33.3 m/s is ~2.1%. The random variations in the peer control variables of velocity (groove depth, temperature, and velocity) appear to have some effect on the gradient of the trend.

The sensitivity trend of C_l with respect to the velocity is shown in Figure 14a. A steady and significant increase (~35%) in C_l is observed by increasing the velocity. The sensitivity trend suggests that by increasing the velocity beyond 33 m/s, a further increase C_l can be expected.

The significance trend of C_l with respect to the velocity is shown in Figure 14b. The reduction gradient of the significance trend of C_d between the velocity values 18.6 and 33.3 m/s is ~12% which is the half of the gradient of the significance trend. The random variations in the peer control variables of velocity (groove depth, temperature, and velocity) appear to have a significant effect on the gradient of the trend.

Table 4. Summary of percentage approximation of changes in C_d and C_l values in sensitivity trends

Control variables	Percentage change in C_d (%)	Control variables	Percentage change in C_l (%)
Groove depth	3.2	Groove depth	21
Groove width	6.8	Groove width	41
Temperature	0.7	Temperature	4.2
Velocity	3.9	Velocity	35

The sensitivity and the significance analyses give insightful information about the aerodynamics of tire model. Hobeika *et al.* (2013) studied tread style as a design parameter and showed that treads are an important factor in aerodynamics of tires. A more in-depth study (how tread dimension effect aerodynamics of tire) is presented in this research work. These results show that the coefficient of drag and coefficient of lift vary with the

https://doi.org/10.1017/S0890060419000039 Published online by Cambridge University Press

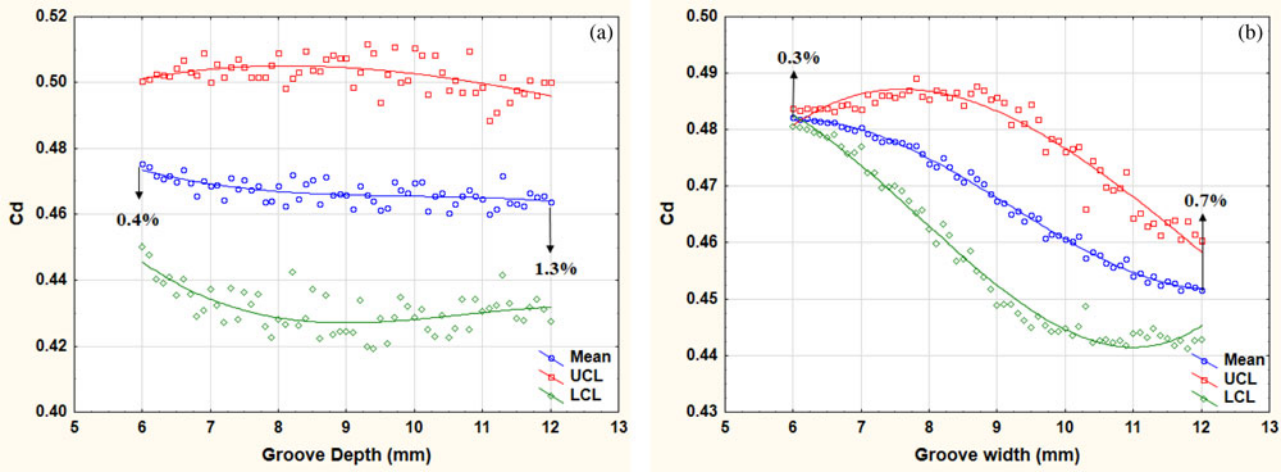


Fig. 15. Paired interaction analysis: (a) C_d versus groove depth with randomly varying groove width and (b) C_d versus groove depth with randomly varying groove depth.

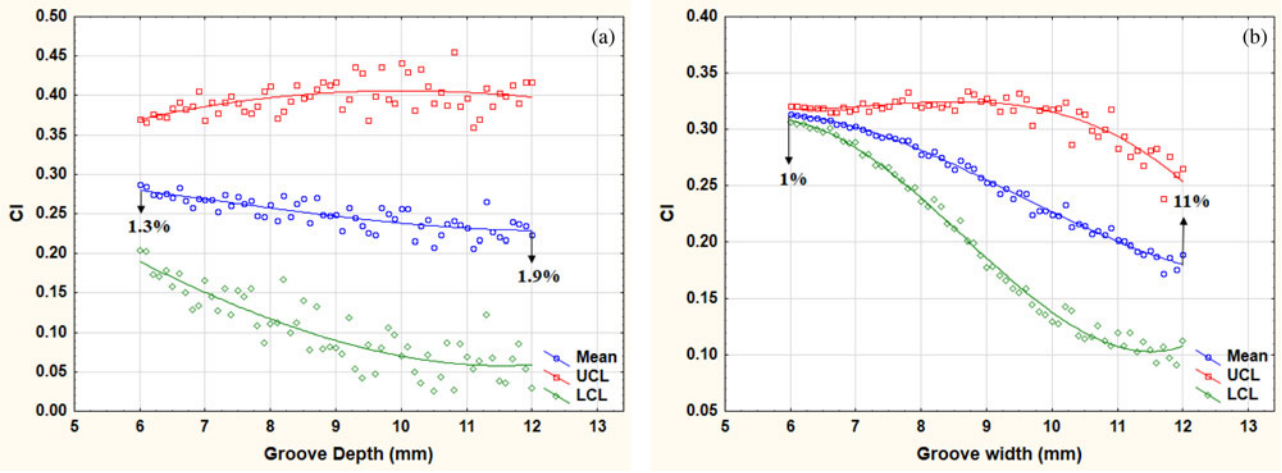


Fig. 16. Paired interaction analysis: (a) C_l versus groove depth with randomly varying groove width and (b) C_l versus groove depth with randomly varying groove depth.

change in velocity as confirmed by previous research (Vdovin, 2015; Leśniewicz *et al.*, 2016). The reduction in C_d is expected to reduce the overall contribution of tire geometry on vehicle drag and in turn on fuel consumption. The reduction in C_l is expected to reduce the overall contribution of tire geometry to vehicle stability and in turn better steering and road safety. The comparison of significance among the control variables is decided based on a detailed study of sensitivity analysis and significance analysis. A summary of approximate percentage change of output variables with respect to the input variables in sensitivity analysis is given in Table 4. The comparison between Figures 7b, 9b, 11b, 13b confirms that the order of significance of the control variables with respect to coefficient of drag is (a) groove width, (b) velocity, (c) groove depth, and (d) temperature. The comparison between Figures 8b, 10b, 12b, 14b confirms that the order of significance of the control variables with respect to coefficient of lift is (a) groove width, (b) velocity, (c) groove depth, and (d) temperature. Furthermore, in most of the previously reported literature, C_d and C_l are considered to be constant at all velocities while testing for variables like tire grooves, etc. This research reveals that the velocity can have a significant impact on C_d and C_l, that is, 4% and 35%, respectively, per tire. Therefore, it may not be considered insignificant for studies relating to contribution of tires in aerodynamic drag and steering stability.

Paired interaction analysis

The paired interaction analyses of important pairs are discussed in this section. In case of paired interaction trend; if the trend lines of the particular variable's corresponding sensitivity trend are unchanged in paired interaction graph, then its paired variable has no effect on the behavior of that particular variable. In this paired interaction study, a qualitative assessment in the shift of trend lines is made by considering the edges of both paired interaction graphs and its corresponding sensitivity graph. An approximate percentage change in the value of edges is calculated and mentioned to understand the extent of interaction between the concerned interacting variable and the corresponding output variable (C_d and C_l).

https://doi.org/10.1017/S0890060419000039 Published online by Cambridge University Press

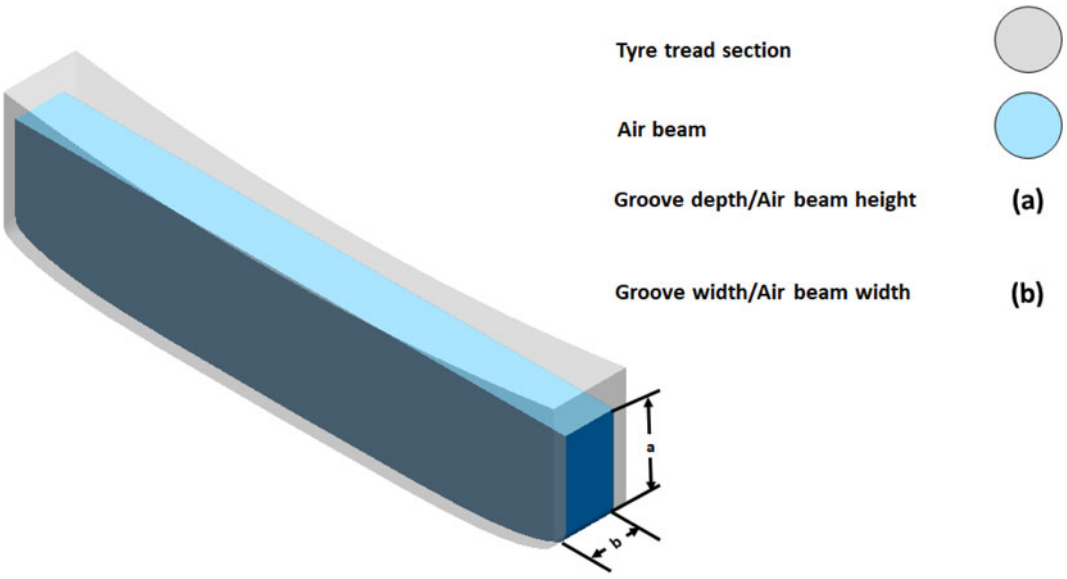


Fig. 17. Section of single groove forming air beam in contact with the road surface.

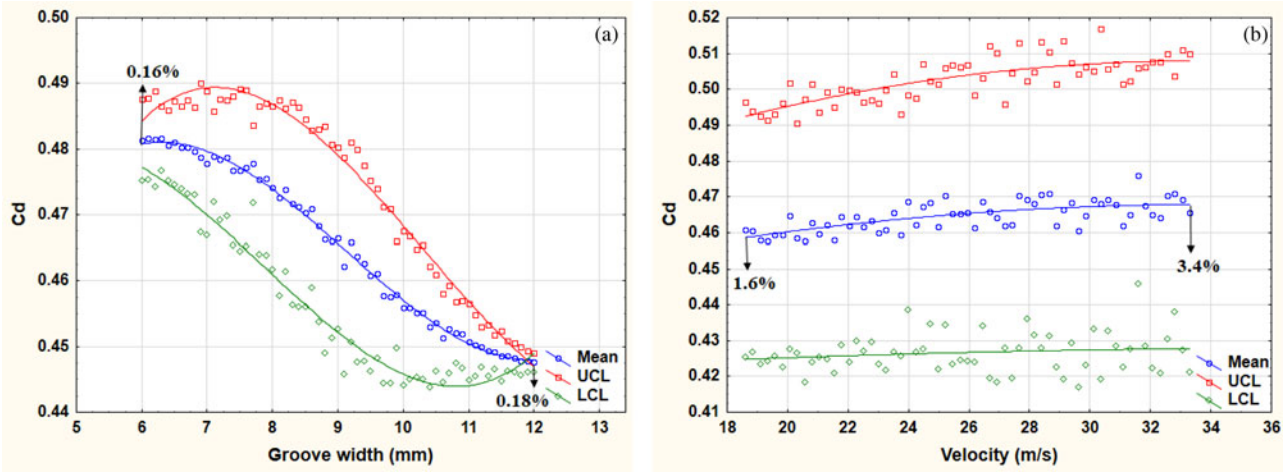


Fig. 18. Paired interaction analysis: (a) C_d versus groove width with randomly varying velocity and (b) C_d versus velocity with randomly varying groove width.

Groove depth and groove width

The paired interaction analyses between groove depth and groove width, with respect to C_d and C_l, respectively, are shown in Figures 15, 16. The percentage increase or decrease values at the extreme ends shown are calculated based on the corresponding values from sensitivity trends in Figures 7a, 8a, 9a, 10a.

Nearly insignificant increase of 0.3% and 0.7% at the edges of Figure 15b reveal that there is almost no interactive effect of groove depth on the strong dependence of tire aerodynamic drag (C_d) on groove width. However, a significant ~11% increase at the higher end of Figure 16b is observed. This shows strong interaction between the control variables groove depth and groove width in terms of C_l; consequently, having significant possible impact on stability. The air entrapped between the groove of the tire and the road acts as an air beam as shown in Figure 17. This entrapped air acts like a typical beam as its impact on C_l (stability) increases as the groove depth/the air beam height increases. A similar kind of higher strength behavior along the greater cross-sectional dimension of general beams is observed in engineering applications which is explained by the section modulus in beam theory.

Groove width and velocity

The paired interaction analyses between groove width and velocity, with respect to C_d and C_l, respectively, are shown in Figures 18, 19. The percentage increase or decrease values at the extreme ends shown are calculated based on the corresponding values from sensitivity trends in Figures 9a, 10a, 13a, 14a.

Again, the insignificant change of 0.16% and 0.18% at the edges of Figure 18a and 1.4% and 1.2% at the edges of Figure 19a reveals that there is almost no interactive effect of velocity on the strong dependence of tire aerodynamic drag (C_d) and aerodynamic lift (C_l) on groove width. However, a significant 1.6%–3.4% and 9.3%–10% decrease at the extreme ends of Figures 18b, 19b is observed. This shows strong interaction between the control variables groove width and velocity in

https://doi.org/10.1017/S0890060419000039 Published online by Cambridge University Press

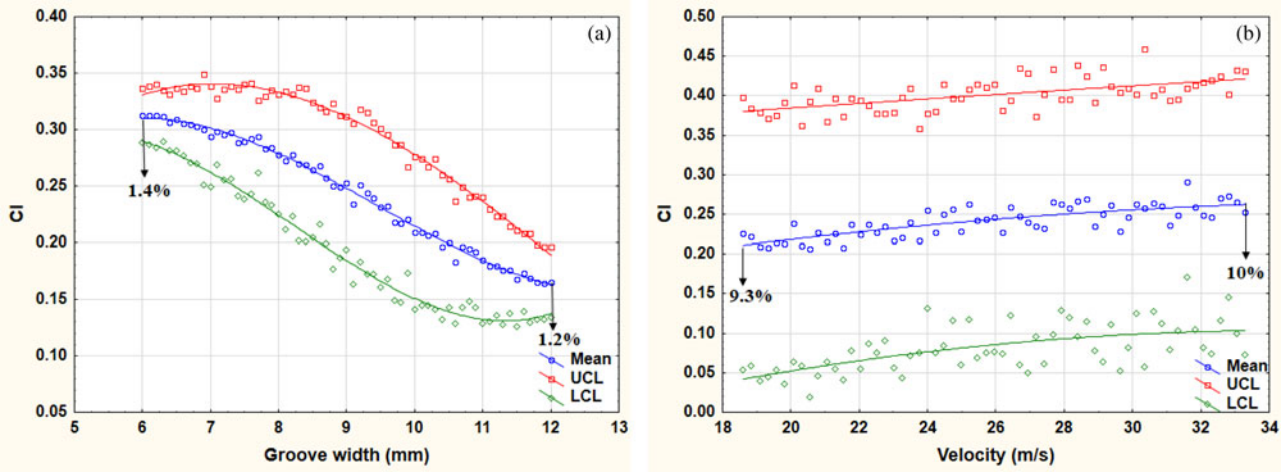


Fig. 19. Paired interaction analysis: (a) C_l versus groove width with randomly varying velocity and (b) C_l versus velocity with randomly varying groove width.

terms of C_d and C_l; consequently, having significant impact on stability.

Conclusion

(i) Neural networks offer a very effective model to study any non-linearity in causal relationships of tire aerodynamics.

(ii) The Monte-Carlo analysis on neural network process models can help conduct the parametric analysis.

(iii) The tight confidence interval of the sensitivity trends reinforces the robustness of the neural network model.

(iv) The order of the significance of the control variables for both C_d and C_l is groove width > velocity > groove depth > temperature. Therefore, the mixing of design parameters and operational parameters is imperative for CFD studies related to tire aerodynamics.

(v) This research also emphasizes that at different velocities the coefficient of drag and the coefficient of lift cannot be considered as constant.

(vi) Increasing the groove depth can help reduce the C_d by ~4% and C_l by ~20%. However, the possibility of reduction in the coefficient of drag and coefficient of lift is very low after 11 mm.

(vii) Increasing the groove width can help reduce the C_d by ~7% and C_l by ~40%. The possibility of further reduction in C_d appears to diminish beyond the range of 12–13 mm. However, the possibility of reduction in the C_l is possible beyond that range and may be considered for investigation in future research.

(viii) The change in design parameters (groove depth and groove width) has a considerable impact on both drag and lift and in turn can have an impact on fuel savings and stability, respectively.

(ix) The negligible significance of the control variable the temperature reveals that the results may be considered independent of the effect of seasonality.

(x) The groove width and the groove depth both have proven to be a strongly interacting pair of control variables with respect to both C_d and C_l.

(xi) The air trapped between the tire groove and the road acts as a beam and exhibits the behavior similar to the concept of section modulus in beam theory.

(xii) The effect of cross wind, different groove types, and number of grooves still needs to be investigated. This work is limited to straight air flow (entering air flow is 90° to z-axis) and with only three longitudinal grooves.

Future work

For further research, design parameters and operational parameters of an isolated tires with different configurations of treads especially, longitudinal grooves with shoulder grooves may be studied. A similar kind of study may be conducted for the inlet air flow from a range of directions such that the angle between the inlet air and z-axis is not equal to 90°.The computer-simulated experiments, MLP-based neural network process model, and Monte-Carlo analysis coupling may also be used to study variable behavior in other components of cars like spoilers, under-tray, and diffusers, etc. The change in C_d and C_l suggest that a similar type of study should be conducted for acoustic analysis and aquaplaning of an isolated tire as well as acoustic analysis and aquaplaning for tires in cars.

References

Abohela I, Hamza N and Dudek S (2013) Effect of roof shape, wind direction, building height and urban configuration on the energy yield and positioning of roof mounted wind turbines. *Renewable Energy* **50**, 1106–1118.

Ahmad NE, Abo-Serie EF and Gaylard A (2010) Mesh optimization for ground vehicle aerodynamics. *CFD Letters* **2**, 54–65.

Ansys I (2016) Ansys Fluent Theory Guide 17.0.

Axerio-Cilies J and Iaccarino G (2012) An aerodynamic investigation of an isolated rotating Formula 1 wheel assembly. *Journal of Fluids Engineering* **134**, 121101.

Axerio-Cilies J, Issakhanian E, Jimenez J and Iaccarino G (2012) An aerodynamic investigation of an isolated stationary formula 1 wheel assembly. *Journal of Fluids Engineering* **134**, 021101.

Axon L, Garry K and Howell J (1998) An evaluation of CFD for modelling the flow around stationary and rotating isolated wheels. *SAE Technical Paper*, No. 980032.

Barberousse A, Franceschelli S and Imbert C (2009) Computer simulations as experiments. *Synthese* **169**, 557–574.

Blocken B and Toparlar Y (2015) A following car influences cyclist drag: CFD simulations and wind tunnel measurements. *Journal of Wind Engineering and Industrial Aerodynamics* **145**, 178–186.

Çengel YA (2010) *Fluid Mechanics*. New Delhi, India: Tata McGraw Hill Education Private.

https://doi.org/10.1017/S0890060419000039 Published online by Cambridge University Press

Collin C, Indinger T and Müller J (2017) Moving ground simulation for high performance race cars in an automotive wind tunnel. *International Journal of Automotive Engineering* **8**, 15–21.

Dang TP, Gu Z and Chen Z (2015) Numerical simulation of flow field around the race car in case: stationary wheel and rotating wheels. *International Journal of Numerical Methods for Heat & Fluid Flow* **25**, 1896–1911.

Das P, Tsubokura M, Matsuuki T, Oshima N and Kitoh K (2013) Large eddy simulation of the flow-field around a full-scale heavy-duty truck. *Procedia Engineering* **56**, 521–530.

Defraeye T, Blocken B, Koninckx E, Hespel P and Carmeliet J (2010) Computational fluid dynamics analysis of cyclist aerodynamics: performance of different turbulence-modelling and boundary-layer modelling approaches. *Journal of Biomechanics* **43**, 2281–2287.

Diasinos S, Doig G and Barber T (2014) On the interaction of a racing car front wing and exposed wheel. *The Aeronautical Journal* **118**, 1385–1407.

Diasinos S, Barber TJ and Doig G (2015) The effects of simplifications on isolated wheel aerodynamics. *Journal of Wind Engineering and Industrial Aerodynamics* **146**, 90–101.

Diasinos S, Barber TJ and Doig G (2017) The influence of wing span and angle of attack on racing car wing/wheel interaction aerodynamics. *Journal of Fluids Engineering* **139**, 061102.

Dieselnet (2018) *Emission Test Cycles* [Online]. Available at http://www.dieselnet.com/standards/cycles (Accessed January 14 2018).

Doig G and Barber TJ (2011) Considerations for numerical modeling of inverted wings in ground effect. *AIAA Journal* **49**, 2330–2333.

European Parliament and Council (2014) European Parliament and Council Regulation (EU) no 540/2014 on the sound level of motor vehicles and of replacement silencing systems and amending directive 2007/46/EC and repealing directive 70/157/EEC. *Official Journal of the European Union*, pp. 131–195.

Fackrell JE (1974) "*The Aerodynamics of an Isolated Wheel Rotating in Contact With the Ground*," University of London, London, U.K.

Fackrell JE and Harvey JK (1973) The Flow Field and Pressure Distribution of an Isolated Road Wheel, Advances in Road Vehicle Aerodynamics. *BHRA Fluid Engineering Conference-Paper*, Vol. 10.

Fackrell JE and Harvey JK (1975) The aerodynamics of an isolated road wheel. *Proceedings of the Second AIAA Symposium of Aerodynamics of Sports and Competition Automobiles, Los Angeles, California, USA* 11, pp. 119–125.

Gérardin F, Gentric C and Midoux N (2014) Particle dispersion in the near-wake of an isolated rotating wheel: experimental and CFD study. *Journal of Aerosol Science* **76**, 56–71.

Grabowski L, Baier A, Buchacz A, Majzner M and Sobek M (2015) Application of CAD/CAE class systems to aerodynamic analysis of electric race cars. *IOP Conference Series: Materials Science and Engineering* **95**, 012044.

Haag L, Blacha T and Indinger T (2017) Experimental investigation on the aerodynamics of isolated rotating wheels and evaluation of wheel rotation models using unsteady CFD. *International Journal of Automotive Engineering* **8**, 7–14.

Heo H, Ju J, Kim DM and Kim H (2014) A computational study of the flow around an isolated Non-pneumatic tire. SAE International Journal *of* Passenger Cars–Mechanical Systems **7**, 405–412.

Hobeika T, Sebben S and Landstrom C (2013) Investigation of the influence of tyre geometry on the aerodynamics of passenger cars. SAE International Journal *of* Passenger Cars–Mechanical Systems **6**, 316–325.

Holder JM, Malla B and Gutmark EJ (2018) CFD Analysis on Single Expansion Ramp Nozzle Performance. *2018 AIAA Aerospace Sciences Meeting*, p. 1099.

Hughes RI (1999) The Ising model, computer simulation, and universal physics. *Ideas In Context* **52**, 97–145.

Issakhanian E, Elkins CJ, Lo KP and Eaton JK (2010) An experimental study of the flow around a formula one racing car tire. *Journal of Fluids Engineering* **132**, 071103.

Kellar WP, Pearse SR and Savill AM (1999) Formula 1 car wheel aerodynamics. *Sports Engineering* **2**, 203–212.

Knowles RD (2005) Mnoposto Racecar Wheel Aerodynamic: Investigation of Near-Wake Structure and Supporting Sting-Interference (Phd). Cranfield University.

Knowles R, Saddington A and Knowles K (2002) On the near wake of rotating, 40%-scale Champ Car wheels, *SAE Technical Paper*, No. 2002-01-3293.

Landström C, Löfdahl L and Walker T (2009) Detailed flow studies in close proximity of rotating wheels on a passenger car. *SAE International Journal of Passenger Cars–Mechanical Systems* **2**, 861–874.

Landström C, Sebben S and Löfdahl L (2010) Effects of wheel orientation on predicted flow field and forces when modelling rotating wheels using CFD. *8th MIRA International Vehicle Aerodynamics Conference*, Vol. **1**, pp. 457–470.

Landström C, Josefsson L, Walker T and Löfdahl L (2011) An experimental investigation of wheel design parameters with respect to aerodynamic drag. *Progress in Vehicle Aerodynamics and Thermal Management 8th FKFS Conference*, pp. 121–136.

Landstrom C, Josefsson L, Walker T and Lofdahl L (2012) Aerodynamic effects of different tire models on a sedan type passenger car. *SAE International Journal of Passenger Cars–Mechanical Systems* **5**, 136–151.

Lanfrit M (2005) Best practice guidelines for handling Automotive External Aerodynamics with FLUENT. Fluent Deutschland GmbH, 64295 Darmstadt/Germany. https://www.southampton.ac.uk/~nwb/lectures/GoodPracticeCFD/Articles/Ext_Aero_Best_Practice_Ver1_2.pdf

Leśniewicz P, Kulak M and Karczewski M (2014) Aerodynamic analysis of an isolated vehicle wheel. *Journal of Physics: Conference Series* **530**, 012064.

Leśniewicz P, Kulak M and Karczewski M (2016) Vehicle wheel drag coefficient in relation to travelling velocity – CFD analysis. *Journal of Physics: Conference Series* **760**, 012014.

Lew C, Gopalaswamy N, Shock R, Duncan B and Hoch J (2017) Aerodynamic Simulation of a Standalone Rotating Treaded Tire, *SAE Technical Paper*, No. 2017-01-1551.

Liang J and Du R (2007) Model-based fault detection and diagnosis of HVAC systems using support vector machine method. *International Journal of Refrigeration* **30**, 1104–1114.

Maxxis (2018) *Maxxis International* [Online]. Available at http://international.maxxis.com (Accessed January 14 2018).

Mcmanus J and Zhang X (2005) A computational study of the flow around an isolated wheel in contact with the ground. *ASME. Journal of Fluids Engineering* **128**, 520–530.

Mears AP, Dominy RG and Sims-Williams DB (2002) The Flow About an Isolated Rotating Wheel-Effects of Yaw on Lift, Drag and Flow Structure, *4th MIRA Int. Vehicle Aerodynamics Conf., Warwick, UK.*

Modlinger F, Demuth R and Adams N (2008) New directions in the optimization of the flow around wheels and wheel arches. *7th MIRA International Vehicle Aerodynamics Conference*, p. 15–16.

Saddington AJ, Knowles R and Knowles K (2007) Laser Doppler anemometry measurements in the near-wake of an isolated Formula One wheel. *Experiments in Fluids* **42**, 671.

Schütz T (2013) *Hucho-Aerodynamik des Automobils: Strömungsmechanik, Wärmetechnik, Fahrdynamik, Komfort*, Springer-Verlag.

Sebben S and Landström C (2011) Prediction of Aerodynamic Drag for Different Rim Designs Using Varied Wheel Modelling in CFD. *Progress in Vehicle Aerodynamics and Thermal Management 8th FKFS Conference*, pp. 1–14.

Shih T-H, Liou WW, Shabbir A, Yang Z and Zhu J (1995) A new k-ϵ eddy viscosity model for high Reynolds number turbulent flows. *Computers & Fluids* **24**, 227–238.

Strumolo GS and Babu V and Ford Global Technologies LLC (2000) Method and system for providing a virtual wind tunnel. U.S. Patent 6,088,521.

Tsanas A and Xifara A (2012) Accurate quantitative estimation of energy performance of residential buildings using statistical machine learning tools. *Energy and Buildings* **49**, 560–567.

Uddin GM, Ziemer KS, Sun B, Zeid A and Kamarthi S (2013) Monte Carlo study of the high temperature hydrogen cleaning process of 6H-silicon carbide for subsequent growth of nano scale metal oxide films. *International Journal of Nanomanufacturing* **9**, 407–430.

Uddin GM, Ziemer KS, Zeid A and Kamarthi S (2015*a*) Monte Carlo study of the molecular beam epitaxy process for manufacturing magnesium oxide nano-scale films. *IIE Transactions* **47**, 125–140.

https://doi.org/10.1017/S0890060419000039 Published online by Cambridge University Press

Uddin GM, Ziemer KS, Zeid A and Kamarthi S (2015*b*) Process model-based analysis of highly crystalline and chemically pure molecular beam epitaxy of MgO (111) nano-thin films on 6H-SiC (0001) substrates. *International Journal of Nanomanufacturing* **11**, 25–45.

Van Den Berg M and Zhang X (2009) The aerodynamic interaction between an inverted wing and a rotating wheel. *Journal of Fluids Engineering* **131**, 101104.

Vdovin A (2015) *Numerical and Experimental Investigations on Aerodynamic and Thermal Aspects of Rotating Wheels*. Gothenburg, Sweden: Chalmers University of Technology.

Vdovin A, Bonitz S, Landstrom C and Lofdahl L (2013) Investigation of wheel ventilation-drag using a modular wheel design concept. SAE International Journal *of* Passenger Cars–Mechanical Systems **6**, 308–315.

Wang S, Burton D, Herbst AH, Sheridan J and Thompson MC (2018) The effect of the ground condition on high-speed train slipstream. *Journal of Wind Engineering and Industrial Aerodynamics* **172**, 230–243.

Watkins S, Saunders JW and Hoffmann PH (1995) Turbulence experienced by moving vehicles. *Part I. Introduction and turbulence intensity. Journal of Wind Engineering and Industrial Aerodynamics* **57**, 1–17.

Wickern G, Zwicker K and Pfadenhauer M (1997) Rotating wheels-their impact on wind tunnel test techniques and on vehicle drag results, *SAE Technical Paper*, No. 970133.

Zhou H, Soh YC and Wu X (2015) Integrated analysis of CFD data with K-means clustering algorithm and extreme learning machine for localized HVAC control. *Applied Thermal Engineering* **76**, 98–104.

Ghulam Moeen Uddin is an Assistant Professor at the Mechanical Engineering Department, University of Engineering and Technology, Lahore. His area of expertise includes machine learning and its applications, tribology, manufacturing process development for semiconductor devices on wide band gap substrates, UHV thin film growth processing and characterization, and wet and dry etching-based surface processing, and chemical and structural characterization. He has published research papers in the areas of surface processing, UHV thin film growth for metal oxides, and developing process control models for optimizing nano-manufacturing processes for transfer from the laboratory to high-volume manufacturing.

Syed Muhammad Arafat is a PhD candidate at the Mechanical Engineering Department, University of Engineering and Technology, Lahore. His research interests include manufacturing process development, design optimization, computational fluid dynamics, and artificial intelligence.

Ali Hussain Kazim is an Assistant Professor at the Mechanical Engineering Department, University of Engineering and Technology, Lahore. His research interests are in the fields of thermodynamics and CFD.

Muhammad Farhan is an Assistant Professor at the Mechanical Engineering Department, University of Engineering and Technology, Lahore. His research interests include computational fluid dynamics and HVAC.

Sajawal Gul Niazi is a graduate student at the Mechanical Engineering Department, University of Engineering and Technology, Lahore. His research interests include computational fluid dynamics and machine learning.

Nasir Hayat is a Professor and currently working as Chairman at the Mechanical Engineering Department, University of Engineering and Technology, Lahore. He holds the PhD degree from Toyohashi University of Technology, Japan. His research interests include manufacturing systems, engineering economic analysis, operational research, and application of artificial intelligence in manufacturing.

Ibrahim Zeid is a Professor of Mechanical and Industrial Engineering at Northeastern University. His research interests include database and information systems in manufacturing, the use of mobile agents to facilitate information access in manufacturing environments, developing XML-based algorithms for mass customization, and developing Java-based and web-based systems for disassembly analysis. Currently his research is focused on scalable nano-manufacturing and engineering education. He has published over 200 papers and secured research grants worth over $3 million.

Sagar Kamarthi is a Professor of Mechanical and Industrial Engineering at Northeastern University. His research interests are in the areas of advanced manufacturing, scalable nano-manufacturing, machine learning, process monitoring and diagnosis, and intelligent sensors/sensor integration. He has published more than 160 articles in internationally reputed journals and has secured several grants from the the National Science Foundation. He has secured research grants worth over $3.5 million. His current research focuses on scalable manufacturing of nano-enabled products.

https://doi.org/10.1017/S0890060419000039 Published online by Cambridge University Press